AGU PUBLICATIONS

JGR

Journal of Geophysical Research: Space Physics

RESEARCH ARTICLE

10.1002/2014JA019809

Key Points:
- Developed numerical model of precipitation
- Evaluate effect of particle phase trapping on precipitation
- Compare nonlinear precipitation model to linear theory

Correspondence to:
V. Harid,
vharid@stanford.edu

Citation:
Harid, V., M. Gołkowski, T. Bell, and U. S. Inan (2014), Theoretical and numerical analysis of radiation belt electron precipitation by coherent whistler mode waves, *J. Geophys. Res. Space Physics*, *119*, doi:10.1002/2014JA019809.

Received 21 JAN 2014
Accepted 29 APR 2014
Accepted article online 7 MAY 2014

Theoretical and numerical analysis of radiation belt electron precipitation by coherent whistler mode waves

V. Harid[1], M. Gołkowski[2], T. Bell[1], and U. S. Inan[1,3]

[1]Department of Electrical Engineering, Stanford University, Stanford, California, USA, [2]Department of Electrical Engineering, University of Colorado Denver, Denver, Colorado, USA, [3]Department of Electrical Engineering, Koc University, Istanbul, Turkey

Abstract The interaction between coherent whistler mode waves and energetic radiation belt electrons can result in pitch angle scattering of electrons into the bounce loss cone and subsequent precipitation. In studying the effects of VLF transmitter signals on particle precipitation, past modeling efforts have focused on the computation of diffusion coefficients for a Fokker-Planck model. In contrast, to capture the nonlinear effects of large-amplitude coherent waves, we evaluate particle precipitation using a Vlasov-Liouville (VL) model which computes the phase space particle distribution function directly using a characteristic-based solution of the Vlasov equation. Previous work has shown that in the case of large-amplitude coherent waves, phase trapping can significantly perturb resonant particles from their adiabatic paths. We evaluate the importance of phase trapping over a range of wave amplitudes (up to 200 pT); the percentage of particles that precipitate after being phase trapped is computed over a phase space grid in the loss cone. The results demonstrate that phase trapping contributes significantly to precipitation when a large-amplitude wave (>100 pT) is present. Additionally, linear theory can be valid over a broad range of amplitudes and the relative accuracy of linear theory in calculating the precipitated flux depends strongly on the initial particle distribution. Additionally, we demonstrate the ability of the VL model to calculate the time evolution of the precipitated flux due to short-duration whistler mode pulses. The physical parameters used in this study are typical of those associated with the Siple Station wave injection experiment.

1. Introduction

Plasma waves in the magnetosphere play an important role in the dynamics of the Earth's radiation belts. The interaction between energetic electrons and plasma waves has been studied extensively over the past 50 years [*Helliwell*, 1965; *Bell and Buneman*, 1964; *Kennel and Petschek*, 1966; *Lyons et al.*, 1972; *Omura et al.*, 1991; *Bortnik et al.*, 2008; *Gendrin*, 1981]. In modeling wave-particle interactions, two general classes of waves are usually considered: incoherent sources and coherent sources. A common incoherent signal is magnetospheric hiss. For precipitation studies, magnetospheric chorus is often treated as an incoherent source as well even though discrete chorus elements are assumed to be coherent in wave amplification and generation studies [*Omura et al.*, 2008], highlighting the rich diversity of the phenomenon. Coherent waves are usually encountered when studying scattering due to signals from VLF communication transmitters or other wave injection sources (such as Siple Station or High Frequency Active Auroral Research Program) [*Helliwell*, 1988; *Gołkowski et al.*, 2008, 2010, 2011]. Regardless of the wave structure, the most fundamental physical description of the interaction requires correctly modeling wave amplification while self-consistently capturing the evolution of the particle distribution. The full treatment of amplification and scattering is a difficult problem that requires solving the Vlasov-Maxwell system of equations [*Nunn*, 1974]. The Vlasov equation dictates the time evolution of a particle distribution in phase space $(\vec{r}, \vec{v})$. Maxwell's equations, on the other hand, determine the evolution of any possible waves in the plasma. Simultaneously solving these equations would describe general plasma behavior. Several authors have used Vlasov-Maxwell solvers to model wave growth [*Omura and Nunn*, 2011; *Gibby et al.*, 2008; *Katoh and Omura*, 2007; *Hikishima et al.*, 2010]; however, measuring particle precipitation in the same numerical model can be difficult to do accurately. This is because wave growth models require solving the Vlasov equation everywhere along the field line and wave growth is dominated by electrons with high pitch angles. On the other hand, precipitation is due to low pitch angle particles falling into the loss cone at the exit of the interaction region.

To quantify particle scattering, many authors consider simplified models where the wave generation mechanism is neglected. That is, waves are assumed to be generated by transmitters or by some unidentified mechanism [*Lyons*, 1974]. If the density of energetic particles is small, wave growth is negligible and this assumption of "no feedback" is valid. The wave propagation characteristics are governed by the background cold, magnetized plasma while the hot plasma (radiation belt electrons) is simply scattered by the incoming waves. A common method of evaluating particle scattering is through quasi-linear theory and the calculation of diffusion coefficients [*Kennel and Petschek*, 1966; *Inan et al.*, 1978; *Abel and Thorne*, 1998; *Albert*, 1999; *Summers*, 2005].

Quasi-linear theory involves a perturbative expansion of the Vlasov equation along with averaging the (generally assumed to be incoherent) wave fields [*Kennel and Engelmann*, 1966]. With these approximations, the Vlasov equation is transformed into a Fokker-Planck diffusion equation in pitch angle, energy, and momentum. This method has been used by numerous authors to model wave-particle interactions by coherent as well as turbulent sources [*Lyons et al.*, 1972; *Steinacker and Miller*, 1992; *Albert*, 1999, 2003; *Glauert and Horne*, 2005]. For instance, this diffusion model has been successfully used to explain the emptying of the slot region during periods of quiet geomagnetic activity [*Lyons et al.*, 1972]. Pitch angle diffusion due to plasmaspheric hiss has been used in several numerical models [*Summers*, 2005]. The primary advantage of this method is that the diffusion coefficients can be calculated numerically (or in some cases analytically) [*Lyons*, 1974; *Albert*, 1994; *Shprits et al.*, 2006; *Tao et al.*, 2012], for a given wave power spectral density. The primary disadvantage of quasi-linear theory is that it is formally valid only for small amplitude, incoherent signals. Nevertheless, it has been used to model scattering by coherent sources as well [*Inan*, 1987; *Albert*, 2001]. In the case of coherent, large-amplitude waves, the diffusive treatment is harder to justify [*Inan et al.*, 1978]. *Albert* [2001] showed that under certain limits, scattering by monochromatic waves can be diffusive and that quasi-linear theory is valid in this regime. However, the general treatment of nonlinear scattering (and precipitation) by large-amplitude coherent waves may not be correctly handled by quasi-linear theory in which case the solution to the Vlasov equation should be computed directly. *Inan et al.* [1978] computed precipitated fluxes due to monochromatic waves by using a semi-Vlasov solver. Although their model solved the nonlinear equations of motion to calculate pitch angle change, gyrophase dependence was neglected when reconstructing the energetic particle distribution function. For large-amplitude waves, phase bunching and phase trapping are important aspects of the nonlinear process [*Dysthe*, 1971; *Matsumoto and Omura*, 1981; *Bell*, 1984; *Gibby et al.*, 2008; *Nunn*, 1974; *Albert et al.*, 2012]; it is therefore more appropriate to use a model that retains the gyrophase dependence of the particle distribution function to correctly model the physics.

Since a large body of previous work has focused on quasi-linear theory, this study is important for evaluating precipitation in the regime where strongly nonlinear effects cannot be neglected. Additionally, the work in this report has important implications for future studies on controlled precipitation of radiation belt electrons. Controlled precipitation can be useful for scientific studies of the upper atmosphere *Inan et al.* [1978]. Additionally, enhanced radiation belt flux levels damage spacecraft yielding an additional motivation for controlled precipitation [*Inan et al.*, 2003].

Recent observations of chorus amplitudes on Time History of Events and Macroscale Interactions during Substorms (THEMIS) [*Li et al.*, 2011] show values of up to 300 pT indicating the need to understand the effects of very large amplitude waves especially since chorus waves are capable of precipitating energetic electrons [*Lorentzen et al.*, 2001]. Although current VLF transmitters do not routinely inject such large-amplitude waves into the magnetosphere, a thorough theoretical understanding would benefit any future projects on controlled precipitation.

In this study, we address three main points in regard to precipitation by coherent waves. First, we discuss numerical modeling of precipitation using a characteristic-based solution to the Vlasov equation (Vlasov-Liouville model). Second, we evaluate the net effect of phase trapping on precipitation, which is a phenomenon that has often been neglected in modeling precipitation. Third, we compute the dependence of precipitated flux on wave amplitude (up to 200 pT) and compare it to linear scattering theory for different hot plasma distribution functions. We also discuss the uses of the Vlasov-Liouville model in simulating the time evolution of the precipitated flux induced by short-duration whistler mode pulses (0.5 s in this study).

The next two sections will discuss theoretical aspects of coherent wave-particle interactions as well as numerical modeling of particle precipitation by coherent waves using the Vlasov-Liouville model. Section 4 describes the results of numerical simulations. Concluding remarks are provided in section 5.

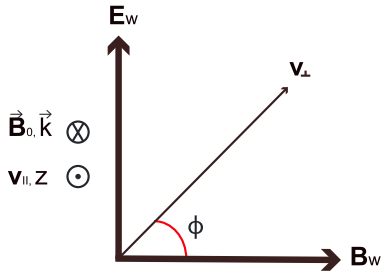

Figure 1. The geometry describing the interaction process. The wave-normal vector k of the whistler mode wave is parallel to the background field; the wave field components, $\vec{B}_w$ and $\vec{E}_w$, are perpendicular to the direction of propagation. The quantities $\vec{v}_{\parallel}$ and $\vec{v}_{\perp}$ are the components of the velocity vector parallel and perpendicular to the background field. The gyrophase angle ϕ is the angle between $\vec{v}_{\perp}$ and $\vec{B}_w$.

2. Theoretical Background

The complete interaction between particles and waves should include every relevant plasma wave mode and any arbitrary direction of propagation. However, for simplicity, we consider only parallel-propagating whistler mode signals. This is a very reasonable assumption for signals that are guided by field-aligned density irregularities, known as "ducts." In these cases, waves will generally propagate nearly parallel to the background geomagnetic field [*Haque et al.*, 2011; *Angerami*, 1970]. Since one of the objectives of this study is to determine precipitation induced by injected signals, the previous assumptions are particularly useful. These assumptions are also used in numerical modeling that shall be discussed in the next section.

The equations of motion (Lorentz force) used are shown in (1)–(4).

$$\frac{dz}{dt} = v_{\parallel} \tag{1}$$

$$\frac{dp_{\parallel}}{dt} = \frac{q}{m\gamma} B_w p_{\perp} \sin\phi - \frac{p_{\perp}^2}{2\gamma\omega_c m}\frac{\partial\omega_c}{\partial z} \tag{2}$$

$$\frac{dp_{\perp}}{dt} = -q\sin\phi(B_w v_{\parallel} + E_w) + \frac{p_{\perp}p_{\parallel}}{2\gamma\omega_c m}\frac{\partial\omega_c}{\partial z} \tag{3}$$

$$\frac{d\phi}{dt} = -k(v_{\text{res}} - v_{\parallel}) - \frac{q\cos\phi}{p_{\perp}}(B_w v_{\parallel} + E_w) \tag{4}$$

The quantities $p_{\perp}$ and $p_{\parallel}$ are the components of the electron's momentum perpendicular and parallel to the background geomagnetic field. The gyrophase angle, ϕ, is the angle between $\vec{p}_{\perp}$ and $-\vec{B}_w$ (antiparallel to wave magnetic field). The terms ω_c, v_{res}, and γ represent the gyrofrequency, resonance velocity and the relativistic Lorentz factor respectively. Nonlinear scattering by coherent waves has been investigated by numerous authors using (1)–(4) either in their current form or by using their nonrelativistic approximations [*Dysthe*, 1971; *Roux and Pellat*, 1978; *Inan et al.*, 1978; *Matsumoto and Omura*, 1981; *Bell*, 1984]. These equations describe the interaction between relativistic electrons and whistler mode waves immersed in a background inhomogeneous magnetic field. The inhomogeneity of the background field is taken into account as a gradient term in (2) and (3). The problem geometry is shown in Figure 1.

In general, when the doppler-shifted wave frequency experienced by the particle equals a multiple of the gyrofrequency ($n\frac{\omega_c}{\gamma} = \omega + kv_{\parallel}$), the particle can resonate with the wave and subsequently undergo a large degree of scattering. Equivalently, if an electron travels at the correct velocity, i.e., the resonance velocity, it will experience an approximately constant value of the wave field. Under the approximation of parallel-propagating whistler mode waves, the $n = 1$ condition is most important, and the resonance velocity is defined by (5).

$$v_{\text{res}} = \frac{\frac{\omega_c}{\gamma} - \omega}{k} \tag{5}$$

The quantities ω and k represent the wave frequency and wave number and are related by the usual cold plasma dispersion relation.

In the absence of a wave field, the mirror force (geomagnetic field) dictates the motion of particles, and the trajectories are adiabatic. For a given equatorial value of $(v_{\parallel}, \alpha)$, the adiabatic particle trajectory can intersect the gyroresonance curve $v_{\text{res}}(z)$ at only two points on the field line for a dipole background magnetic field and diffusive equilibrium cold plasma density model [*Inan et al.*, 1978].

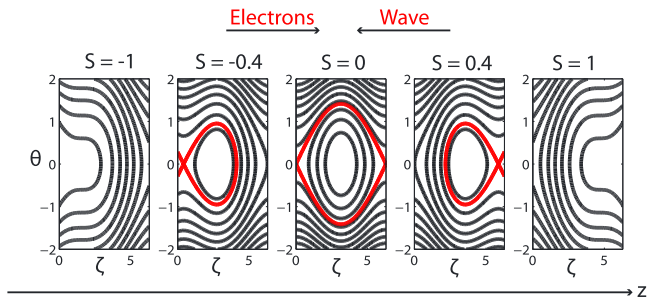

Figure 2. Instantaneous single particle trajectories in (θ, ζ) coordinates for an inhomogeneous background field and monochromatic wave ($\zeta = -\phi$). Here $\theta = \frac{k(v_{res}-v_{\|})}{\omega_{tr}\sqrt{2}}$ and represents a normalized change from the resonance velocity. The formation of a separatrix and phase space trap is clearly visible within the region delineated by the red curves. The phase space trap is a function of position along the field line. At the equator, the phase space trajectories correspond to the homogenous case; however, away from the equator, the trap decrease in size and the stable phase (center of trap) drifts as well. Far enough from the equator, no trap exists at all and the nonlinear wave effects become negligible. The trajectories shown correspond to $-1 < S < 1$.

An important consequence of equations (1)–(4) is phase trapping and the formation of a separatrix in phase space. This concept has been studied by several authors and continues to be a topic of active research [*Dysthe*, 1971; *Nunn*, 1974; *Inan et al.*, 1978; *Matsumoto and Omura*, 1981; *Park*, 1981; *Albert*, 2002; *Gibby et al.*, 2008; *Omura et al.*, 2008; *Tao et al.*, 2012]. To describe the dynamics of resonant electrons, we follow the procedure of *Omura et al.* [2008]. For simplicity, particles of nonrelativistic energies are considered; however, the same framework applies for the relativistic regime. If only particles that are close to resonance are examined and the small contribution of centripetal acceleration due to the wave is neglected, equations (2) and (4) (introducing $\zeta = -\phi$) can be simplified to (6) and (7),

$$\frac{d\zeta}{dt} = k(v_{res} - v_{\|}) \tag{6}$$

$$\frac{d^2\zeta}{dt^2} - \omega_{tr}^2 (\sin\zeta + S) = 0 \tag{7}$$

Where ω_{tr} is the trapping frequency and is given by $\sqrt{\frac{q}{m}B_w k v_\perp}$. S is the "collective inhomogeneity factor" [*Omura et al.*, 1991] and is given by (8),

$$S = \frac{1}{\omega_{tr}^2}\left[\frac{kv_\perp^2}{2\omega_c} + \frac{3v_{res}}{2}\right]\frac{\partial\omega_c}{\partial z} \tag{8}$$

The expression for S given in (8) assumes no frequency sweep rate (monochromatic) and assumes a constant plasma frequency. Note that the S parameter in this work is opposite in sign to the one used in *Omura et al.* [1991, 2008], since our waves propagate in the $-z$ direction and not $+z$ as in the those works. For the simplifying case of $S = 0$ (homogenous case), equation (7) is identical to the well-known pendulum equation. That is, the motion of the electron's $\vec{v}_\perp$ about the wave magnetic field, $\vec{B}_w$, is analogous to the motion of a classical pendulum in a constant gravitational field. To illustrate the formation of the separatrix, particle trajectories must be examined in the $(v_{\|}, \phi)$ coordinates. Figure 2 demonstrates the formation of a separatrix (shown by the closed red curves). The separatrix divides the trajectories into two regions: trapped and untrapped. Trapped particle trajectories (interior) form closed curves while the untrapped particle trajectories swing around the separatrix. The formation of this trap is a crucial aspect of coherent wave-particle interactions; the motion of particles in, out, and around the trap describes the nonlinear interaction.

So far, only the simplifying case of $S = 0$ has been examined in equation (7). The inclusion of the inhomogeneity term makes the problem more complex. The concept of phase trapping carries over to the inhomogeneous problem; however, the shape of the trap changes as a function of position along the field line. Figure 2 shows the instantaneous phase space trajectories for a monochromatic signal in an inhomogeneous background field. At the equator, the trajectories are identical to the homogenous case; however, away from the equator, the trap shrinks and the stable phase location changes (center of trap). Far enough from the equator, the trap disappears altogether. Formally, the separatrix can only exist when $-1 < S < 1$. If the background plasma were homogenous ($S = 0$), then the initially trapped particles will stay trapped and untrapped particles will stay untrapped. However, for a spatially dependent S, this is not necessarily

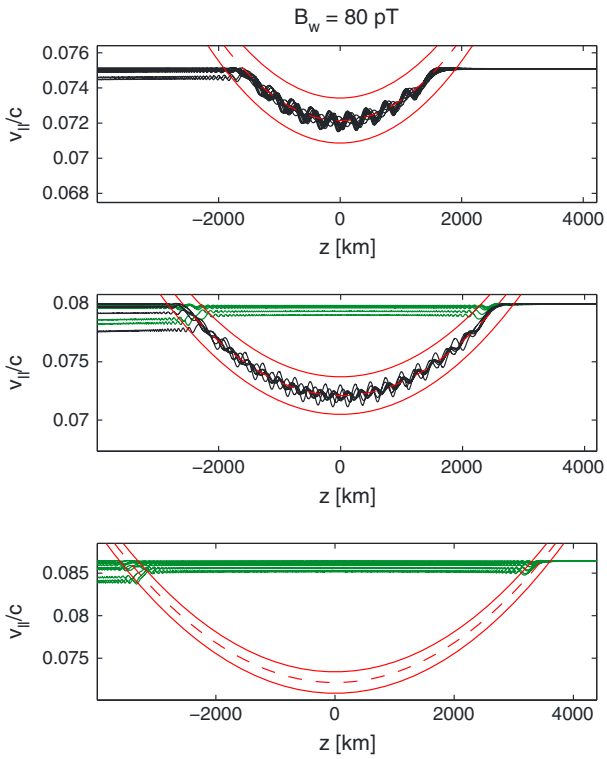

Figure 3. Particle trajectories for 12 particles uniformly distributed in gyrophase. Trapped particles are shown in black while untrapped particles are shown in green. The red dashed curve corresponds to the local resonance velocity while the solid red curves represent bounds of $\pm 1 v_{tr}$ (size of the trap). (top) A case where the particles $v_{\|}$ equals the resonance velocity near the equator and are all trapped. (middle) A smaller percentage of trapped particles since the resonance velocity is encountered farther up the field line. (bottom) Only untrapped particles with no particles being phase trapped; this is because the particles come into resonance much farther up the field line (where $|S| > 1$).

the case. Particles can either swing around the trap or be trapped for many trapping periods before being detrapped. The exact dynamics are strongly dependent on the particles' initial phase angle, energy, and pitch angle [*Inan et al.*, 1978]. This analysis can simplify numerical modeling since the bulk of the nonlinear interaction occurs only in a narrow spatial extent around the equator (where $-1 < S(z) < 1$); however, the size of the interaction region grows with the wave amplitude. Note that trapped and untrapped particles refer to phase-trapped and phase-untrapped particles, respectively, and shall be referred to as such in the remainder of this report.

Figure 3 (middle) shows the trajectories of 12 particles (uniformly distributed in gyrophase) that have the same $v_{\|}$ and α_{eq} at the exit of the interaction region (right-hand side). Figure 3 (middle) identifies the untrapped electrons (green) and the phase-trapped electrons (black). As shown, the instantaneous trajectories of trapped particles significantly deviate from the adiabatic paths and are forced to follow the local resonance velocity curve for multiple trapping periods. Although there is a large change in $v_{\|}$ on one side of the equator, there is an opposite change on the other side leading to smaller net effect. The change in energy and pitch angle for trapped particles has been demonstrated by several authors, and the focus has often been on the interaction in only one hemisphere leading to a less symmetric change [*Tao et al.*, 2013; *Bortnik et al.*, 2008; *Furuya et al.*, 2008; *Inan et al.*, 1978]. Interaction in only one hemisphere is reasonable for waves generated at the equator and propagating away. In the case of a ground-based wave injection experiment (such as Siple Station), the electrons will interact with the wave on both sides of the field line and result in more symmetric phase-trapped trajectories as shown in Figure 3 (at least once the wave fills the simulation space). The corresponding change in pitch angle can be seen in Figure (4). As shown, the pitch angle of a trapped electron will increase (decrease) when the parallel velocity decreases (increases). The reason for this is that the effect of the wave electric field is rather small and phase trapping is due to the wave magnetic field [Inan 1978]. Since magnetic fields can only alter a particle's momentum, this implies that the wave scatters particles with a larger change to the momentum in comparison to the energy. The result is a change in pitch angle opposite in sign to the change in parallel velocity. In section 4, the net pitch angle change is compared in detail for trapped and untrapped particles.

In order to correctly model precipitation for a distribution of particles, a full analytical treatment is not possible and numerical simulations are required. However, the theoretical foundations described in this section provide the general framework for setting up numerical simulations. The next section describes the numerical model used in this study to simulate precipitation of a particle distribution due to coherent waves.

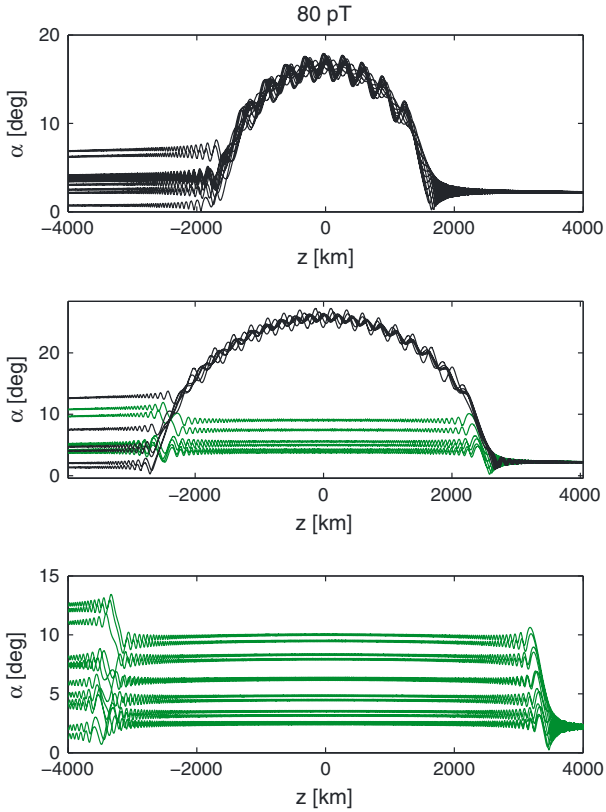

Figure 4. (top–bottom) The instantaneous pitch angle trajectories for the same particles as Figure 3. Trapped particles are shown in black while untrapped particles are shown in green. Note that the peak pitch angle change is very large for trapped particles; however, the net pitch angle change is still similar to that of untrapped particles.

3. Model Description

All simulations are performed using a centered dipole geomagnetic field model, at $L = 4$. We use the cold density model from *Carpenter and Anderson* [1992] to determine the cold plasma parameters under quiet geomagnetic conditions. At $L = 4$, the equatorial gyrofrequency is $f_c = 13.6$ kHz; the simulations use an input wave frequency of $f_0 = f_c/3 = 4.5$ kHz and a cold plasma density of $N_{\text{cold}} = 400$ el/cm^3.

In addition, we assume field-aligned propagation (ducted waves) in the whistler mode. Two families of particle distributions are considered for the energetic electrons. The first is a loss cone bi-Maxwellian distribution which is given by (9)

$$f(p_{\|}, p_{\perp}) = C_b e^{-\frac{p_{\|}^2}{2p_{\text{th}\|}^2}} \left[e^{-\frac{p_{\perp}^2}{2p_{\text{th}\perp}^2}} - e^{-\frac{p_{\perp}^2}{2\beta p_{\text{th}\perp}^2}} \right] \tag{9}$$

The term β is a configurable parameter ($0 < \beta < 1$) such that larger values of β give a more depleted loss cone while $\beta = 0$ is a pure bi-Maxwellian. Additionally, $C_b = \frac{N_h}{(1+\beta) p_{\text{th}\|} p_{\text{th}\perp}^2 (\sqrt{2\pi})^3}$, N_h is the hot plasma density and $p_{\text{th}\|}$ and $p_{\text{th}\perp}$ represent the average momenta (of the hot plasma) parallel and perpendicular to the geomagnetic field. All simulations use $v_{\text{th}\perp} = 0.4c$ and $v_{\text{th}\|} = 0.17c$ unless specifically stated otherwise (where c is the speed of light in free space). The second distribution is a sin-alpha distribution and is given by

$$f(\alpha, p) = C_s \frac{(\sin \alpha)^{\gamma_s}}{p^m} \tag{10}$$

where C_s is a normalization constant. The quantities γ_s and m are configurable parameters that define the distribution. Both distributions assume $f(\alpha < \alpha_{\text{LC}}) = 0$ to ensure an initially empty loss cone. This also ensures zero precipitated flux for zero wave field.

The wave fields are taken into account by illuminating the entrance of the interaction region with an input signal and using this as a boundary condition for the wave equations. Since all the waves in this study exist over a small range of frequencies, the narrowband approximation of Maxwell's equations is used to minimize computational effort. The narrowband wave equation is shown in (11).

$$\frac{\partial B_w}{\partial t} - v_g \frac{\partial B_w}{\partial z} = 0 \tag{11}$$

Here v_g is the group velocity for a parallel-propagating wave in the whistler mode. Equation (11) describes the advection of a wave packet in $-z$ direction with velocity $v_g(z)$. Modified versions of this equation have also been derived by several authors to model coherent wave-particle interactions (generally including a source term) [*Nunn*, 1974; *Omura and Nunn*, 2011; *Gibby*, 2008; *Gibby et al.*, 2008]. Note that equation (11) is used only to save on computational effort; it can be replaced by Maxwell's equations for general (not narrowband) wave fields.

A fourth-order Runge-Kutta (RK4) time-stepping scheme is used to evolve the single particle equations of motion. The wave equation is time stepped using a semi-Lagrangian scheme with cubic spline interpolation.

3.1. Vlasov-Liouville (VL) Model

The Vlasov-Liouville numerical model essentially solves the Vlasov equation for given a wave field at a particular location along the field line. The Vlasov equation governs the evolution of collisionless plasma in phase space $(\vec{r}, \vec{p})$. The Vlasov equation is shown in (12); the terms in parenthesis correspond to equations (1)–(4).

$$\frac{\partial f}{\partial t} + \left(\frac{\mathrm{d}z}{\mathrm{d}t}\right)\frac{\partial f}{\partial z} + \left(\frac{\mathrm{d}p_{\parallel}}{\mathrm{d}t}\right)\frac{\partial f}{\partial p_{\parallel}} + \left(\frac{\mathrm{d}p_{\perp}}{\mathrm{d}t}\right)\frac{\partial f}{\partial p_{\perp}} + \left(\frac{d\phi}{\mathrm{d}t}\right)\frac{\partial f}{\partial \phi} = 0 \tag{12}$$

Since we are only interested in whether particles at the exit of the interaction region fall into the loss cone, it is unnecessary to commit computational resources to solve for the distribution function everywhere along the field line. However, since the Vlasov equation is an advective-type partial differential equation (PDE), information propagates around phase space in a complicated manner. That is, the distribution function at the exit of the interaction region depends on the distribution at many other locations in phase space at previous times.

An accurate method of computing the distribution is by using the method of characteristics, which in the context of the Vlasov equation is equivalent to Liouville's theorem. This is done by considering characteristic curves, which are curves along which the distribution function is advected. This turns the PDE into a set of ODEs. More specifically, consider a general advection equation shown in (13)

$$\frac{\partial f}{\partial t} + \vec{c}(\vec{r})\frac{\partial f}{\partial \vec{r}} = 0 \tag{13}$$

This type of equation describes advection of the quantity $f(t, \vec{r})$ at "speed" $\vec{c}$ at "position" $\vec{r}$. To find the characteristics, we find the trajectories, $\vec{r}(t)$ for which the total derivative vanishes, shown in (14)

$$\frac{\mathrm{d}f(t, \vec{r}(t))}{\mathrm{d}t} = \frac{\partial f}{\partial t} + \frac{d\vec{r}}{\mathrm{d}t}\frac{\partial f}{\partial \vec{r}} = 0 \tag{14}$$

The original advection equation (13) can only be satisfied if (15) is satisfied

$$\frac{\mathrm{d}\vec{r}}{\mathrm{d}t} = \vec{c} \tag{15}$$

Another interpretation is that in the frame of reference moving at speed $\vec{c}$, the quantity f does not change. Thus, by solving for the trajectories using (15), we find the curves along which f is advected. In the case of the Vlasov equation, the characteristic curves are found by solving (1)–(4). This means the value of the distribution function at any particular point can be determined by tracing the characteristic curves back until time zero. As long as characteristics do not intersect (which is the case for the Vlasov equation), this method works very well. In this method, a grid is generated over $(\phi, v_{\parallel}, \alpha)$ in the loss cone at the exit of the interaction region. The characteristics are traced backward (formally $\mathrm{d}t \rightarrow -\mathrm{d}t$ for the equations of motion and narrowband wave equations) until time zero or until they reach the "entrance" of the interaction region. Similar procedures have been used by previous authors in modeling particle dynamics [*Nunn and Omura*, 2011; *Speiser*, 1965]. It is assumed that the numerical interaction region is large enough that outside this region the distribution function is essentially unperturbed (one pass precipitation). This allows the simulation to stop before reaching time zero, hence saving on computational time. Therefore, for a sampled set of times, the loss cone distribution function can be obtained. To evaluate precipitation, an integral is computed over the loss cone to obtain a precipitated flux. Since the VL model directly computes the phase space distribution function, characterizing precipitation requires computing the appropriate integral. To quantify precipitation, two different measures are utilized: the precipitated flux F_p in el/m^2 s and the precipitated energy flux E_p in J/m^2 s. Equations (16)–(17) explicitly show the integrals in the $(\alpha, \phi, p_{\parallel})$ coordinate system.

$$F_p = \int\int_0^{\alpha_{\mathrm{LC}}}\int_0^{2\pi} v_{\parallel} f(\alpha, \phi, p_{\parallel}) p_{\parallel}^2 \frac{\sin(\alpha)}{\cos(\alpha)^3}\mathrm{d}\phi\mathrm{d}\alpha\mathrm{d}p_{\parallel} \tag{16}$$

$$E_p = \int\int_0^{\alpha_{\mathrm{LC}}}\int_0^{2\pi} v_{\parallel}(m\gamma c^2 - mc^2) f(\alpha, \phi, p_{\parallel}) p_{\parallel}^2 \frac{\sin(\alpha)}{\cos(\alpha)^3}\mathrm{d}\phi\mathrm{d}\alpha\mathrm{d}p_{\parallel} \tag{17}$$

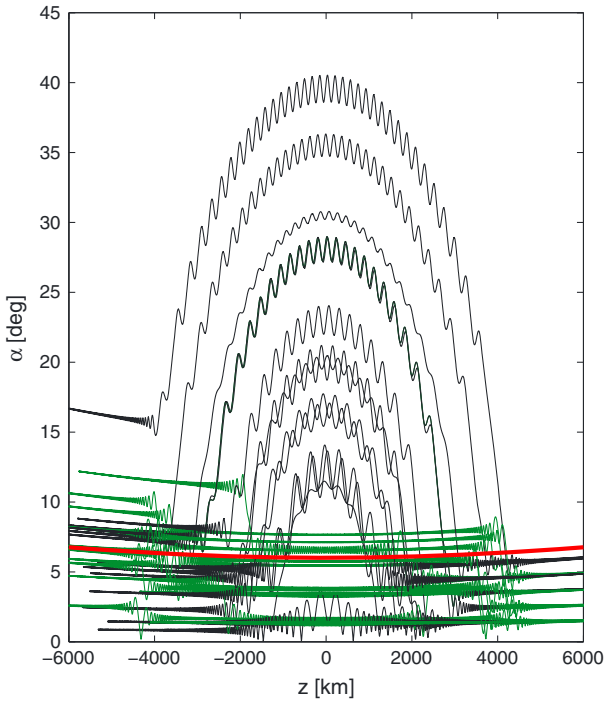

Figure 5. Thirty randomly selected pitch angle trajectories from the Vlasov-Liouville model (B_w = 80 pT). The particles' initial conditions sample the loss cone at the "exit" of the interaction region (right); the trajectories are then tracked backward in time until they reach the entrance of the interaction region (left). Only trajectories that are above the local loss cone angle at the left side of the interaction region contribute to a nonzero precipitated density (for an initially empty loss cone). Trapped particles are shown in black, and untrapped particles are shown in green. The local loss cone is represented by the solid red curve.

Figure 5 shows sample trajectories that demonstrate how the loss cone is being filled at the exit of the interaction region. The actual particle trajectories flow from left to right. However, in the Vlasov-Liouville method, the scattering is performed backward in time, and the trajectories are computed from right to left. As can be seen in Figure 5, particles that end up in the loss cone (on the right) start with various initial pitch angles and can be scattered in complicated ways. The local loss cone is shown in red and is calculated by providing an initial equatorial loss cone pitch angle value and constructing the rest of the curve according to adiabatic motion. All trajectories that start from inside the loss cone (on the left) and end up in the loss cone (on the right) do not contribute to precipitation (at least for an initially empty loss cone). Only particles that start outside the loss cone (on the left) and end up inside the loss cone (on the right) will contribute to precipitation (for an initially empty loss cone).

The VL model requires a grid in phase space, and the range of initial $v_{\|}$ and α must be chosen correctly. The simulations use an interaction region that is approximately ±6000 km around the geomagnetic equator. The phase space grid has $N_{v_{\|}} \times N_\alpha \times N_\phi = 200 \times 50 \times 32 = 320{,}000$ grid points. Since only the precipitated distribution function is of interest, the phase space grid consists of $0 < \alpha < \alpha_{LC}$.

3.2. Comparison to Monte Carlo Simulation

The VL model was chosen to analyze precipitation because the loss cone is very well defined. This way, the phase space grid is created precisely over the loss cone at the exit of the interaction region and the trajectories are traced backward in time until reaching the entrance (or time zero). In this manner, only the trajectories that fall into the loss cone are kept track of, a feature which saves tremendously on computational effort.

In contrast, a more brute force approach would use a Monte Carlo-type simulation. A Monte Carlo model first starts by treating the particle distribution as a probability distribution and sampling it with a number of test particles. Then, the particles are essentially "let go" and are forced to follow the equations of motion. A genuine concern with this model is whether the distribution has been sampled with enough particles to capture the nonlinear effects. This is similar to the concern faced by PIC (particle-in-cell) simulations. Only a fraction of particles fall into the loss cone per time step which means a very large number of particles are necessary to extract the precipitated particle distribution (much higher than the VL model). In PIC simulations of wave-particle interactions, it is not uncommon to use 10^8 superparticles [*Hikishima et al.*, 2010]. Thus, when considering precipitation, the VL model saves on computation by only tracking the relevant trajectories. The VL model has the added advantage of being easily parallelizable. Each particle can be scattered independently, and the time sample when precipitation is measured can be computed in parallel. The VL method is limited by how well the grid is sampled in phase space. However, convergence can easily be determined by simply increasing the number of grid points and verifying that the results are no longer changing (within some tolerance).

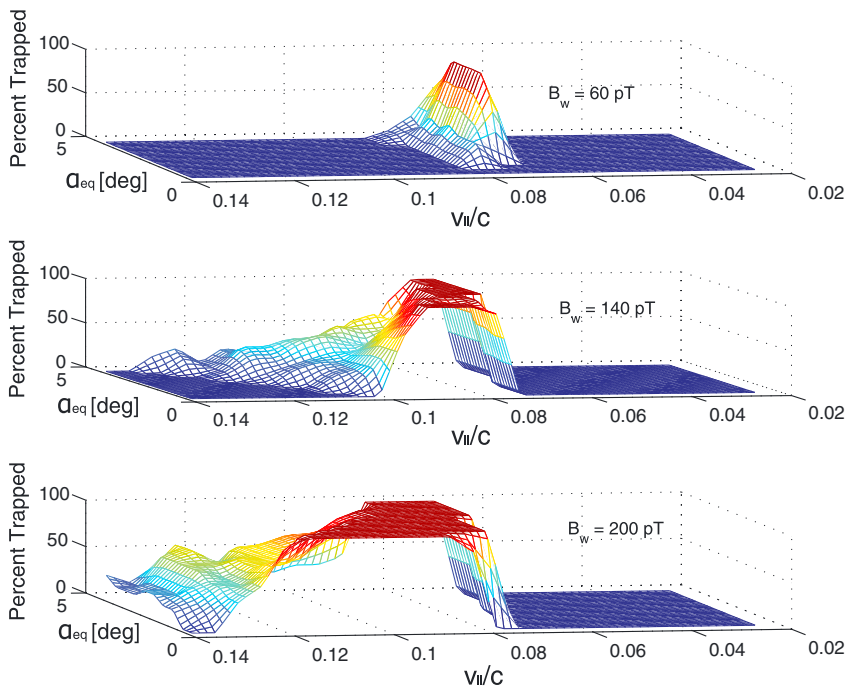

Figure 6. Percent of particles trapped (in gyrophase) as a function of final $(v_{\|}, \alpha_{eq})$ coordinates for three different wave amplitudes (60 pT,140 pT, and 200 pT). As shown, the percentage of particles trapped increases with wave amplitude. As shown, the percentage of particles trapped is high for $v_{\|}$ close to $v_{res}(z_{eq})$ and falls off at higher value of $v_{\|}$; the larger amplitudes allow trapping over a larger portion of phase space. This is precisely because $S(z)$ is small close to the equator and the size of the trap is large; therefore, particles that come into resonance close to the equator have a higher probability of being trapped.

4. Simulation Results

In the following subsections, we address two primary aspects of precipitation induced by coherent waves: (1) The effect of phase trapping on precipitation. (2) Comparison of simulated precipitated flux to linear scattering theory for different initial particle distributions (over $0 < B_w < 200$ pT). The last subsection will demonstrate the ability of the VL model to compute the precipitated particle flux as a function of time for short-duration input pulses.

4.1. Effect of Phase Trapping

As discussed in section 2, resonant particles with certain gyrophase angles can be phase trapped by the wave for multiple trapping periods. The VL model is used to quantify the probability of trapping and the net scattering of phase-trapped particles. A grid is created in phase space $(v_{\|}, \alpha, \phi)$ at the exit of the interaction region, and the characteristics are then traced backward in time. The trajectories of the resonant particles are then categorized as either phase trapped or untrapped. As a search criterion, a trajectory is considered trapped based on the number of crossings of $v_{\|}$ through resonance. That is, untrapped electrons will intersect the resonance curve exactly twice while trapped particles will cross resonance more than twice. Particles with $v_{\|}$ close to $v_{res}(z_{eq})$ will come into resonance close to the equator; since $S(z)$ is smallest near the equator, the likelihood of being phase trapped is high for these particles. Particles with $v_{\|} > v_{res}(z_{eq})$ will come into resonance away from the equator, and the likelihood of trapping decreases (since $S(z)$ is larger). Figure 3 illustrates this concept. Figure 3 (top) shows 12 particles at a lower $v_{\|}$ such that they come into resonance close to the equator (±1800 km). As shown, all the particles are phase trapped. Figure 3 (middle) shows particles that come into resonance farther down the field line (±2500 km); as shown, about half the particles are phase trapped and half untrapped. Figure 3 (bottom) shows particles that come into resonance even farther down from the equator (±3200 km); in this case, none of the particles are phase trapped and all are untrapped. This clearly illustrates the dependence of the likelihood of trapping on final $(v_{\|}, \alpha)$. From Figure 3, it is expected to see a high percentage of trapped particles for velocities close to $v_{res}(z_{eq})$ and a decrease at higher values of $v_{\|}$. Figure 4 shows instantaneous pitch angle trajectories of the same particles as Figure 3.

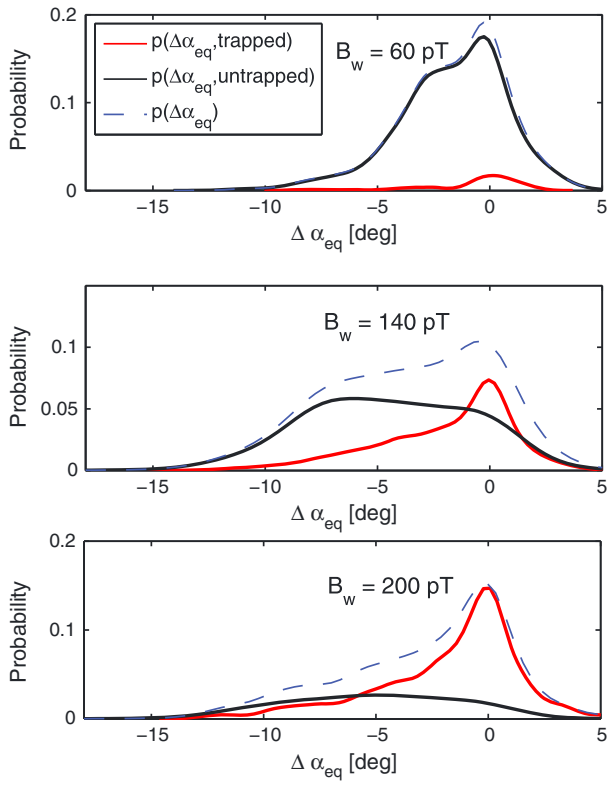

Figure 7. The probability distributions over $\Delta\alpha_{eq}$ for three wave amplitudes. At 60 pT, precipitation is completely dominated by untrapped particles. At 140 pT and 200 pT, there is a visible contribution due to the trapped population. As shown, the effect of phase trapping becomes increasingly important as the wave amplitude is increased and can no longer be considered negligible for evaluating precipitation.

Using the trapping criterion described, the percent of particles that become trapped (in gyrophase) can be computed as a function of $(v_{\|}, \alpha)$. Figure 6 shows the percent of particles trapped as a function of $(v_{\|}, \alpha_{eq})$ for three different wave amplitudes (60 pT, 140 pT, and 200 pT). As shown, the percentage of trapped particles is higher for $v_{\|}$ close to $v_{res}(z_{eq})$ and falls off at larger parallel velocities for all three wave amplitudes. For the 60 pT case, very few particles are trapped in a small range of parallel velocities around $v_{res}(z_{eq})$. For the 140 pT case, a larger percentage of the particle population is trapped with 100% being trapped around $v_{res}(z_{eq})$. For 200 pT, an even larger number of particles are trapped with a 100% likelihood of trapping over a significant portion of phase space. Figure 6 demonstrates how very large amplitude waves can trap a larger number of phase space trajectories; however, the more practical question is how much of the total precipitation is due to trapped particles and how much is due to untrapped particles. Since the trajectories of precipitated particles have been computed over a large number of initial (or rather final) conditions, a probability distribution over equatorial pitch angle change, $p(\Delta\alpha_{eq})$, can also be computed (using kernel density estimation). That is, if the variables $(v_{\|}, \phi)$ are not considered and only the pitch angle change is measured, the quantity $\Delta\alpha_{eq}$ can be treated as a random variable. Here the quantity $\Delta\alpha_{eq}$ is computed by subtracting the equatorial pitch angle at the entrance from the equatorial pitch angle at the exit.

The quantity $p(\Delta\alpha_{eq})$ can be compared to the distributions for trapped and untrapped particles ($p(\Delta\alpha_{eq} \cap \textit{trapped})$ and $p(\Delta\alpha_{eq} \cap \textit{untrapped})$) to see which particle population dominates. Since the untrapped and trapped particle populations are mutually exclusive, $p(\Delta\alpha_{eq}) = p(\Delta\alpha_{eq} \cap \text{trapped}) + p(\Delta\alpha_{eq} \cap \text{untrapped})$.

Figure 7 shows a comparison of the different probabilities for three different wave amplitudes (60 pT, 140 pT, and 200 pT). As shown, for the 60 pT case, $p(\Delta\alpha_{eq} \cap \text{untrapped})$ and $p(\Delta\alpha_{eq})$ are almost identical indicating that the net scattering is effectively due to the untrapped population. At 140 pT, $p(\Delta\alpha_{eq} \cap \text{trapped})$ becomes more important, and at 200 pT, there is a comparable contribution from both the trapped and untrapped population; scattering due to trapping is no longer negligible at such large amplitudes. The results suggest that for large wave amplitudes (greater than 100 pT), phase trapping is an important effect when considering precipitation. Note that all particles in the probability distributions are in the loss cone at the exit of the interaction region. The positive values of $\Delta\alpha_{eq}$ then correspond to trajectories that were already in the loss cone and simply got pushed to a higher pitch angle that is still in the loss cone. These trajectories will not contribute to the precipitated flux for an initial distribution with an empty loss cone.

4.2. Comparison to Linear Theory

For a constant amplitude wave filling the simulation space (CW wave), the precipitated energy flux can be computed. The VL model only requires the computation of one pass through the interaction region for a constant wave field. That is, the particles begin at the exit of the interaction region and are scattered backward in time until they reach the entrance. Due to the spatial symmetry of a constant wave field, the

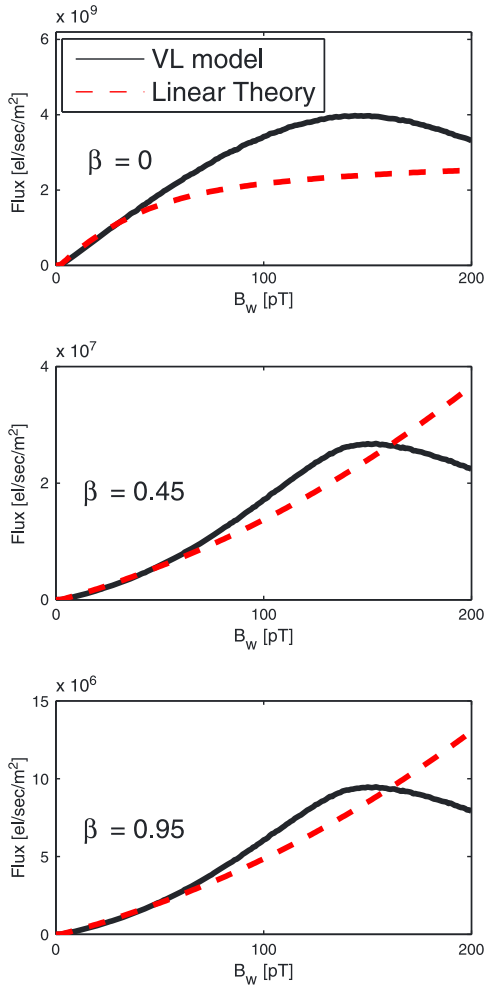

Figure 8. The dependence of precipitated flux on wave amplitude for three different values of β (bi-Maxwellian loss cone parameter). The comparison to linear scattering theory is shown as dashed red curves. As shown, the fluxes due to linear theory and the VL model are similar for small amplitudes; however, as the wave amplitude is increased, the fluxes due linear theory deviate from the full nonlinear model. As shown, the amplitude at which this deviation occurs depends on the initial particle distribution function (parameterized by β).

scattering only needs to be computed once; every pass through the interaction region (with initial conditions over a phase space grid) will result in the same particle trajectories. The distribution function is assumed to be unperturbed at the entrance, and Liouville's theorem is used to determine the precipitated distribution at the exit. The fixed entrance boundary condition is a simplifying assumption used in this model but can be improved upon in future work.

By computing the precipitated flux as a function of amplitude, the results of the model can be compared to linear scattering theory. Linear theory is a perturbative model of the wave-particle interaction phenomenon and is derived under the assumption of "small" wave amplitude. The derivation of expressions for the precipitated flux due to linear theory is presented in the appendix. Since the precipitated flux depends on the particle distribution, we compute the precipitated flux as a function of wave amplitude for different initial distributions (described in section 4). Figure 8 shows the precipitated flux for three different bi-Maxwellian parameters ($\beta = 0$, $\beta = .45$, and $\beta = .95$). Additionally, the precipitated flux due to linear scattering theory is shown for comparison in each panel. As shown, linear theory is valid for low amplitudes and then deviates from the VL model at large amplitudes as expected. An interesting aspect is that how well linear theory matches the nonlinear model depends on the initial particle distribution function (value of β). That is, the error due to the linear theory approximation can be "damped out" depending on the shape of the initial distirbution function. The same comparison can be done for the sin-alpha distribution; this is shown in Figure 9. In this particular case, we use $m = 2$ and vary γ_s ($\gamma_s = 1$, $\gamma_s = 3$, $\gamma_s = 10$). As shown in Figure 9, linear theory matches the VL model for low amplitudes just as with the bi-Maxwellian distribution. Additionally, the range of validity of linear theory once again depends on the initial distribution function (value of γ_s). A general behavior across all the initial distributions is that starting at low amplitudes, the precipitated flux increases with amplitude until a local maximum is reached around 130–140 pT. The flux subsequently decreases for larger amplitudes. Since phase trapping becomes more important at these large amplitudes (as described in the previous section), the decrease in precipitated flux is likely due to the nonlinear contribution of phase-trapped particles. The strength of the VL model is that only the characteristics are tracked; therefore, the initial particle distribution can be arbitrarily specified after the simulation is run. That is, the VL model creates a database of mappings from the exit phase space grid to the initial phase space coordinates. The precipitated flux due to different particle distributions is computed a posteriori. As the results show, the precipitated flux depends strongly on the initial particle distribution. Thus, easily determining the effects of arbitrary particle distributions is an essential aspect of a numerical model of precipitation (specifically for coherent waves).

4.3. Time Evolution of Precipitated Flux

Another aspect of coherent wave-particle interactions that is not often considered is the precipitated flux induced by short pulses. As mentioned previously, *Inan et al.* [1982] and *Chang et al.* [1983] used

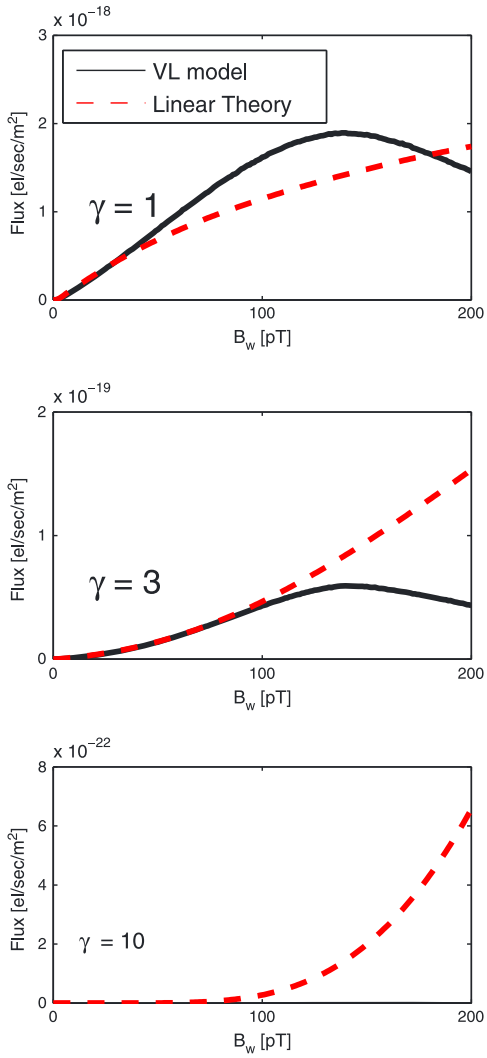

Figure 9. The dependence of precipitated flux on wave amplitude for three different values of γ_s (sin-alpha distribution parameter). The parameter m for the sin-alpha distribution is set to $m = 2$. The comparison to linear scattering theory is shown as dashed red curves. As with the bi-Maxwellian distributions, the fluxes due to linear theory and the VL model are similar for small amplitudes. Once again, the accuracy of linear theory in calculating the precipitated flux depends on the shape of the initial particle distribution (parameterized by γ_s).

a semi-Vlasov model to compute the precipitated fluxes for short pulses. However, their method saved on computational effort by assuming a perturbed distribution function that is uniformly distributed in gyrophase. The VL model used in the present study solves the Vlasov equation and retains the gyrophase dependence.

In the previous sections, only the case of a constant wave amplitude filling the space (CW signal) was discussed. The VL model can also be used to calculate the precipitated flux as a function of time due to short pulses. Specifically, one side of the interaction region is illuminated with the input signal (boundary condition), and the wave then propagates through the interaction region. For each time step, the VL model can be used to trace the system back to time zero and subsequently evaluate the precipitated flux. As mentioned in section 3, the entrance of the interaction region is specified with a fixed boundary condition for the phase space particle distribution. This basically assumes that fresh particles continuously stream into the interaction region. This assumption is valid over time scales for which the initial distribution function is not perturbed significantly. Future iterations of the model can include a time-varying boundary condition to capture the long-term evolution of the particle distribution function; however, that is beyond the scope of the present study. The VL model can accurately be used to model precipitation due to short pulses since the aforementioned assumptions will be valid.

To demonstrate the ability of the VL model to compute the time-dependent precipitated flux, we consider 0.5 s input wave pulses. Additionally, different frequency-time sweep rates (fallers and risers) are considered to resemble signal formats used during the Siple Station wave injection experiment. Rising and falling tones can also closely resemble free-running triggered emissions and discrete chorus elements. The precipitated flux due to short pulses can be complicated since the finite sized wave packet fills only part of the interaction region. Therefore, only a limited range of resonant velocities are available to interact with the wave at any given time. Figure 10 shows the spatial profile of the wave at three different times as well as the range of resonance velocities available for interaction (shown in red). As shown, at $t = 0.399$ s, the wave has partially filled the interaction region; however, since the resonance velocity curve is much steeper away from the equator, a significant range of resonance velocities can interact with the wave. At $t = 0.799$ s, the entire wave packet is within the interaction region and is located near the equator. Close to the equator, the resonance velocity curve is flatter since the inhomogeneity of the background geomagnetic field is small. Consequently, a much smaller range of resonance velocities are available for interaction near the equator. At $t = 1.0667$ s, the wave starts to leave the simulation space and once again has a larger range of resonance velocities available for interaction.

This pattern of a large range of available resonance velocities followed by a small range and then large again is reflected in Figure 11. Figure 11 (bottom) shows the normalized input wave signal as a function of

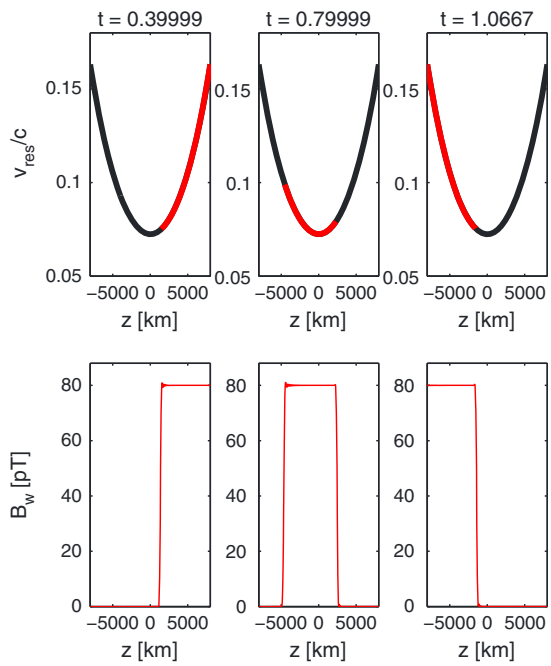

Figure 10. Range of resonance velocities interacting with the wave for $N_c = 400$ el/cm^3 as well as the spatial profile of the wave packet at three different times. Away from the equator, the wave packet can interact with a large range of resonance velocities while only a small range of resonance velocities are available for interaction near the equator. As shown, this effect is due to the shape of the resonance curve.

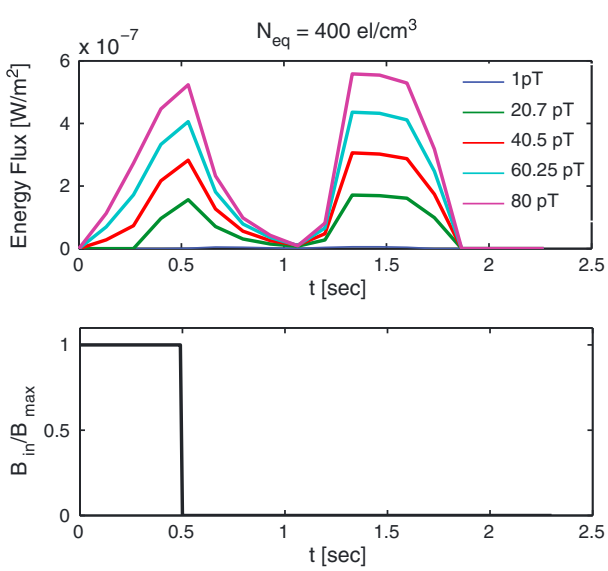

Figure 11. Precipitated energy flux as a function of time due to a 0.5 s pulse for $N_{eq} = 400$ el/cm^3 (over a range of wave amplitudes). Although the input wave pulse lasts 0.5 s, the response of the precipitated energy flux lasts approximately 1.8 s. This extended response time is due to the spread of velocities that can interact with the wave as well as the size of the wave packet within the interaction region (which depends on the input pulse length and group velocity).

time (0.5 s pulse). Figure 11 (top) shows the precipitated energy flux as a function of time due to the pulse for five different wave amplitudes. As shown, there are two peaks in the precipitate energy flux profile (the first at around 0.5 s and the second at approximately 1.4 s). This is due to the different ranges of resonance velocities available for interaction at different times, as discussed earlier. Additionally, the precipitated flux responds for approximately 1.8 s even though the wave pulse was only 0.5 s long. After the particle interacts with the wave, there is a finite time delay before the particle reaches the exit of the simulation space (where precipitation is measured). For instance, a particle in resonance velocity curve at high values of v_{res} inherently has a higher $v_{\|}$ than a particle that intersects the resonance velocity curve close to the equator. As shown in Figure 10, the maximum and minimum resonance velocities in the simulation space differ by a factor of 2. Thus, the two different particles will the reach the exit of the interaction region at different times. This adds to the extended response time of the precipitated flux and illustrates the added complexity of the problem.

Figures 10 and 11 have only considered a high cold plasma density (400 el/cm^3). At high cold plasma densities, the wave group velocity is small which makes the length of the wave packet much smaller; thus, the wave never completely fills the simulation space. At lower cold plasma densities, the group velocity is higher, and the wave packet will simultaneously fill a larger physical region for the same 0.5 s duration input pulse. This is demonstrated in Figure 12. In this lower cold plasma density case (50 el/cm^3), the group velocity is higher and the wave packet can fill the entire simulation space ($t = 0.4$ s). Unlike the high density case, the largest range of resonance velocities are available for interaction once the wave has filled the entire simulation space.

In the low-density case, two peaks in the precipitated energy flux are not expected to happe,n and only one maximum should occur when the wave fills the space. This is evident in Figure 13. Figure 13 (top) shows the precipitated energy flux as a function of time due to the 0.5 s input pulse for five

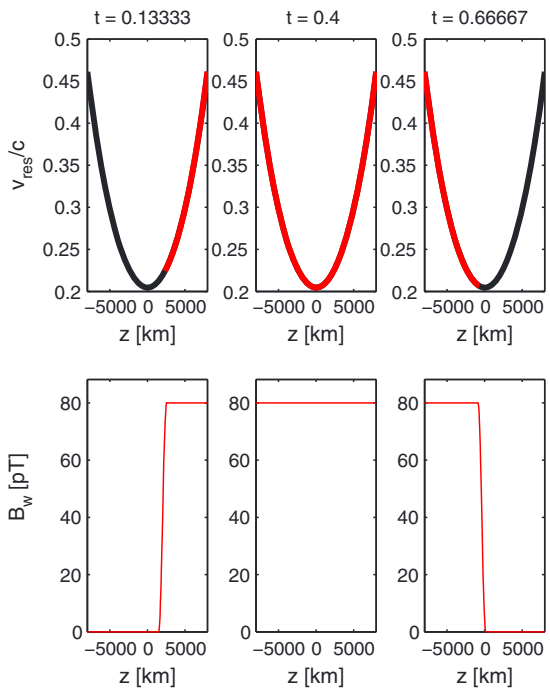

Figure 12. Range of resonance velocities interacting with the wave for $N_c = 50$ el/cm^3 as well as the spatial profile of the wave packet at three different times. At this cold plasma density, the group velocity is large enough that the wave packet can fill the entire simulation space ($t = 0.4$ s) unlike the case of the higher plasma density.

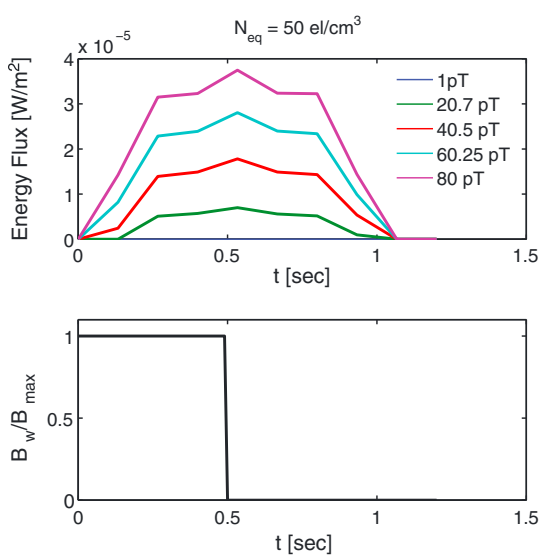

Figure 13. Precipitated energy flux as a function of time due to a 0.5 s pulse for $N_{eq} = 50$ el/cm^3 (over a range of wave amplitudes). Although the input wave pulse lasts 0.5 s, the response of the precipitated energy flux lasts approximately 1.05 s. This extended response time is due to the spread of velocities that can interact with the wave as well as the size of the wave packet within the interaction region (which depends on the input pulse length and group velocity).

different wave amplitudes ($N_{eq} = 50$ el/cm^3). As expected, there is only one maximum in the precipitated energy flux profile which occurs at around $t = 0.55$ s. Additionally, the flux response lasts for approximately 1.05 s. This is less than the high-density case for multiple reasons. Since the wave frequency was kept the same as the high-density case, the resonance velocities are much higher for the low cold plasma density case as shown in Figure 12. Thus, the particles cross the interaction region much faster than in the high-density case which decreases the time delay. The higher group velocity means that the wave will cross the interaction region much faster which also decreases the response time of the precipitated flux.

These results demonstrate the complex nature of the problem when considering precipitation induced by short pulses. As shown, the VL model is well suited to simulate the physics of wave-particle interactions and can be extended to input pulses with a time-varying frequency (specifically rising and falling tones). That is, we consider signals with format $f(t) = f_0 + a_r t$ where f_0 is the initial wave frequency and a_r is the frequency sweep rate in Hz/s (angular acceleration). All simulations use $f_0 = 4.5$ kHz while a_r varies from −2 to 2 kHz/s. Figure 14a shows the precipitated energy flux for falling tones (−2 kHz/s). Figure 14b shows monochromatic pulses while Figure 14c shows the energy flux for rising tones (+2 kHz/s). All three cases use $N_c = 400$ el/cm^3. As shown, the qualitative temporal profiles are similar for all three cases. The value of the precipitated energy flux is highest for the falling frequency case since the falling tone is composed of the lowest frequencies and consequently interacts with higher resonant energies. The purpose of Figure 14 is to demonstrate the ability of the VL model to simulate precipitation induced by coherent waves of changing frequency. Note that an additional equation (apart from equation (11)) is required to propagate the changing frequency signal. For the present study, we used the following approximate wave equation:

$$\frac{\partial \omega}{\partial t} - v_g \frac{\partial \omega}{\partial z} = 0 \tag{18}$$

Equation (18) has only been used for computational simplicity and can be replaced by Maxwell's equations if necessary.

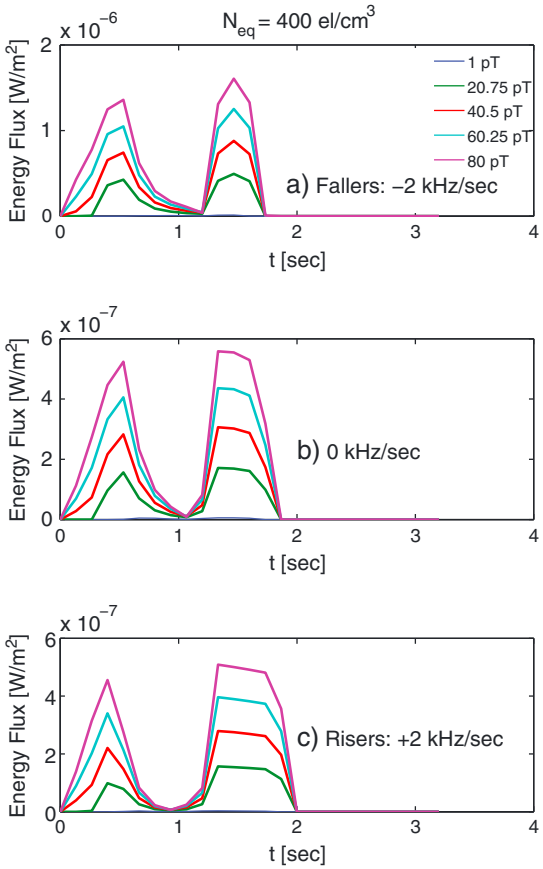

Figure 14. Precipitated energy flux as a function of time due to a 0.5 s pulses with different frequency sweep rates (N_{eq} = 400 el/cm^3). The temporal profiles of all three cases are qualitatively similar. As shown, the falling tone induces the highest precipitated energy flux since the lower frequency components interact with higher resonant energies.

5. Summary and Discussion

In this report we have addressed multiple questions regarding precipitation by coherent signals using a novel Vlasov-Liouville numerical model. We considered the effect of phase trapping on precipitation. Using the VL model, we computed the probability distribution over pitch angle change for precipitated particles. The results show that phase trapping becomes an important effect as the wave amplitude is increased to large values (>100 pT). The precipitated flux predicted by linear scattering theory was compared to the VL model as a function of wave amplitude (for various hot plasma distributions). Linear scattering theory was shown to be valid for small wave amplitudes (<40–60 pT); however, the point of deviation of linear theory from the nonlinear model (when computing the precipitated flux) depends strongly on the initial hot plasma distribution function.

Finally, the ability of the VL model to simulate precipitation induced by 0.5 s pulses with changing frequency was demonstrated. The complicated temporal response of the precipitated flux suggests that maximizing precipitation may require a nontrivial input wave format. Formally, finding the ideal input wave format would require a solution to a PDE-constrained optimization problem. That is, the problem would be to maximize the integrated precipitated flux subject to the Vlasov equation, wave equations, and any other practical constraints (such as amplitude limit and sweep rate limit). The optimum wave format can be selected by using the appropriate optimization methods. For known cold plasma parameters and a known background field, the general optimization problem is difficult but is likely solvable with modern computational tools. The theoretical and numerical analysis presented in this report can be used as a stepping stone toward optimizing controlled particle precipitation and analyzing nonlinear wave-particle interactions.

Appendix A: Linear Scattering Theory

Linear scattering theory involves expanding the equations of motion around the adiabatic particle trajectories. In particular, the equations of motion can be written as

$$\frac{d\vec{p}}{dt} = \vec{F}_w + \vec{F}_a \tag{A1}$$

Where the quantities $\vec{p}$, $\vec{F}_a$, and $\vec{F}_w$ represent the particle state, the "force" due to adiabatic motion, and the force due to the wave respectively. In particular, they are given by

$$\vec{p} = \begin{pmatrix} p_{\parallel} \\ p_{\perp} \\ \phi \\ z \end{pmatrix},$$

$$\vec{F}_w = \begin{pmatrix} qB_w v_\perp \sin\phi \\ -q\sin\phi(B_w v_\parallel + E_w) \\ 0 \\ 0 \end{pmatrix},$$

$$\vec{F}_a = \begin{pmatrix} -\frac{p_\perp^2}{2\gamma\omega_c m}\frac{\partial\omega_c}{\partial z} \\ \frac{p_\perp p_\parallel}{2\gamma\omega_c m}\frac{\partial\omega_c}{\partial z} \\ k(v_{\text{res}} - v_\parallel) \\ v_\parallel \end{pmatrix},$$

Additionally, the state vector can be written as $\vec{p} = \vec{p}_a + \Delta\vec{p}$, where $\vec{p}_a$ is the adiabatic motion of the particle state (when no wave is present) and $\Delta\vec{p}$ is the wave-induced perturbation to the particle state. So far, the only approximation has been neglecting the additional wave force term on the phase variation which is very small for magnetospheric parameters. The linearization step is introduced by expanding the forces in a power series around adiabatic motion.

$$\frac{\mathrm{d}\vec{p}_a}{\mathrm{d}t} + \frac{\mathrm{d}\Delta\vec{p}}{\mathrm{d}t} = \vec{F}_w(\vec{p}_a) + \vec{F}_a(\vec{p}_a) + \frac{\partial\vec{F}_w}{\partial\vec{p}_a}(\Delta\vec{p}) + \frac{\partial\vec{F}_a}{\partial\vec{p}_a}(\Delta\vec{p}) + O(\Delta p^2) \tag{A2}$$

Where $\frac{\partial\vec{F}}{\partial\vec{p}_a}$ is the 4×4 Jacobian matrix evaluated at $\vec{p}_a$. Linear scattering theory involves only taking the lowest order terms in $\Delta\vec{p}$ which involves only the zero-order terms in this case. Additionally, $\frac{\mathrm{d}\vec{p}_a}{\mathrm{d}t} = \vec{F}_a$ by definition. The perturbation due to linear theory is then given by

$$\frac{\mathrm{d}\Delta\vec{p}}{\mathrm{d}t} = \vec{F}_w(\vec{p}_a) \tag{A3}$$

In component form, linear theory is given by

$$\frac{\mathrm{d}\Delta p_\parallel}{\mathrm{d}t} = qB_w v_{\perp_a}\sin\phi_a \tag{A4}$$

$$\frac{\mathrm{d}\Delta p_\perp}{\mathrm{d}t} = -q(B_w v_{\parallel_a} + E_w)\sin\phi_a \tag{A5}$$

All terms with the subscript "a" correspond to adiabatic motion. For the case where a constant amplitude monochromatic wave is filling the entire simulation space (CW signal), the linearized equations of motion can be parameterized by position instead of time. In this case, linear theory is given by

$$\frac{\mathrm{d}\Delta p_\parallel}{\mathrm{d}z} = \frac{qB_w v_{\perp_a}\sin\phi_a}{v_{\parallel_a}} \tag{A6}$$

$$\frac{\mathrm{d}\Delta p_\perp}{\mathrm{d}z} = \frac{-qB_w(v_{\parallel_a} + v_p)\sin\phi_a}{v_{\parallel_a}} \tag{A7}$$

These equations can be integrated to obtain $\Delta p_\perp$ and $\Delta p_\parallel$ as a function of position along the field line. These can be obtained numerically or in some cases analytically [*Inan*, 1987]. However, in the spirit of the VL model, the scattering can be calculated for one pass through the interaction region. For "final" coordinates at the exit ($+z_L$) of the interaction region, the "initial" perturbations at the entrance ($-z_L$) are given by

$$\Delta p_\parallel(-z_L) = \Delta p_\parallel(z_L) - \int_{-z_L}^{z_L} \frac{qB_w v_{\perp_a}\sin\phi_a}{v_{\parallel_a}}\mathrm{d}z \tag{A8}$$

$$\Delta p_\perp(-z_L) = \Delta p_\perp(z_L) - \int_{-z_L}^{z_L} \frac{-qB_w(v_{\parallel_a} + v_p)\sin\phi_a}{v_{\parallel_a}}\mathrm{d}z \tag{A9}$$

To specify the boundary conditions, we choose $\vec{p}(z_L) = \vec{p}_a(z_L) + \Delta\vec{p}(z_L) = \vec{p}_a(z_L)$ so that $\Delta\vec{p} = 0$. Note that this is not an approximation; since there are two free parameters ($\vec{p}_a(z_L)$ and $\Delta\vec{p}(z_L)$), it is simply a convenient choice that states that perturbations are chosen relative to the final particle coordinates. Nonzero values of $\Delta\vec{p}(z_L)$ will be reflected as a different value of $\vec{p}_a(z_L)$. Therefore, the scattering of one pass through the interaction region predicted by linear theory for a constant amplitude monochromatic wave is given by

$$\Delta p_{\parallel}(-z_L) = -B_w \int_{-z_L}^{z_L} \frac{q v_{\perp_a} \sin\phi_a}{v_{\parallel_a}} \mathrm{d}z \tag{A10}$$

$$\Delta p_{\perp}(-z_L) = B_w \int_{-z_L}^{z_L} \frac{q(v_{\parallel_a} + v_p) \sin\phi_a}{v_{\parallel_a}} \mathrm{d}z \tag{A11}$$

Next, using Liouville's theorem, the distribution function at the exit can be computed in terms of the initial distribution function at the entrance,

$$f(p_{\parallel}(z_L), p_{\perp}(z_L), \phi(z_L), z_L) = f_{-z_L}(p_{\parallel}(-z_L), p_{\perp}(-z_L)) \tag{A12}$$

Here $p(-z_L) = \vec{p}_a(-z_L) + \Delta\vec{p}(-z_L)$. However, for a model that is symmetric around the geomagnetic equator (as used in this study), $\vec{p}_a(-z_L) = \vec{p}_a(z_L)$. And as stated, earlier, the boundary conditions enforce $\vec{p}_a(z_L) = \vec{p}(z_L)$. Therefore, equation (A12) can be rewritten as

$$f(p_{\parallel}(z_L), p_{\perp}(z_L), \phi(z_L), z_L) = f_{-z_L}\left(p_{\parallel}(z_L) + \Delta p_{\parallel}(-z_L), p_{\perp}(z_L) + \Delta p_{\perp}(-z_L)\right) \tag{A13}$$

Dropping all the (z_L) terms (since it is implied) and explicitly including the perturbations gives

$$f(p_{\parallel}, p_{\perp}, \phi, z_L) = f_0\left(p_{\parallel} - B_w \int_{-z_L}^{z_L} \frac{q v_{\perp_a} \sin\phi_a}{v_{\parallel_a}} \mathrm{d}z, p_{\perp} + B_w \int_{-z_L}^{z_L} \frac{q(v_{\parallel_a} + v_p) \sin\phi_a}{v_{\parallel_a}} \mathrm{d}z\right) \tag{A14}$$

The subscript "$-z_L$" has been replaced by the subscript "0" to indicate an initially unperturbed distribution. Once the distribution is computed, the precipitated flux can then be calculated by integrating over phase space as shown in equations (16) and (17).

Acknowledgments
This work has been supported by AFRL award FA9453-11-C-0011 to Stanford University.

Michael Liemohn thanks the reviewers for their assistance in evaluating this paper.

References

Abel, B., and R. M. Thorne (1998), Electron scattering loss in Earth's inner magnetosphere: 1. Dominant physical processes, *J. Geophys. Res.*, *103*, 2385–2396, doi:10.1029/97JA02919.

Albert, J. (2002), Nonlinear interaction of outer zone electrons with VLF waves, *Geophys. Res. Lett.*, *29*(8), 1275, doi:10.1029/2001GL013941.

Albert, J. M. (1994), Quasi-linear pitch angle diffusion coefficients: Retaining high harmonics, *J. Geophys. Res.*, *99*(A12), 23,741–23,745, doi:10.1029/94JA02345.

Albert, J. M. (1999), Analysis of quasi-linear diffusion coefficients, *J. Geophys. Res.*, *104*(A2), 2429–2441, doi:10.1029/1998JA900113.

Albert, J. M. (2001), Comparison of pitch angle diffusion by turbulent and monochromatic whistler waves, *J. Geophys. Res.*, *106*(A5), 8477–8482, doi:10.1029/2000JA000304.

Albert, J. M. (2003), Evaluation of quasi-linear diffusion coefficients for EMIC waves in a multispecies plasma, *J. Geophys. Res.*, *108*(A6), 1249, doi:10.1029/2002JA009792.

Albert, J. M., X. Tao, and J. Bortnik (2012), Aspects of nonlinear wave-particle interactions, in *Dynamics of the Earth's Radiation Belts and Inner Magnetosphere, Geophys. Monogr. Ser.*, vol. 199, edited by D. Summers et al., pp. 255–264, AGU, Washington, D. C., doi:10.1029/2012GM001324.

Angerami, J. J. (1970), Whistler duct properties deduced from VLF observations made with the OGO 3 satellite near the magnetic equator, *J. Geophys. Res.*, *75*(31), 6115–6135, doi:10.1029/JA075i031p06115.

Bell, T. F. (1984), The nonlinear gyroresonance interaction between energetic electrons and coherent VLF waves propagating at an arbitrary angle with respect to the Earth's magnetic field, *J. Geophys. Res.*, *89*(A2), 905–918, doi:10.1029/JA089iA02p00905.

Bell, T. F., and O. Buneman (1964), Plasma instability in the whistler mode caused by a gyrating electron stream, *Phys. Rev.*, *133*, A1300–A1302, doi:10.1103/PhysRev.133.A1300.

Bortnik, J., R. M. Thorne, and U. S. Inan (2008), Nonlinear interaction of energetic electrons with large amplitude chorus, *Geophys. Res. Lett.*, *35*, L21102, doi:10.1029/2008GL035500.

Carpenter, D. L., and R. R. Anderson (1992), An ISEE/whistler model of equatorial electron density in the magnetosphere, *J. Geophys. Res.*, *97*, 1097–1108, doi:10.1029/91JA01548.

Chang, H. C., U. S. Inan, and T. F. Bell (1983), Energetic electron precipitation due to gyroresonant interactions in the magnetosphere involving coherent VLF waves with slowly varying frequency, *J. Geophys. Res.*, *88*, 7037–7050, doi:10.1029/JA088iA09p07037.

Dysthe, K. B. (1971), Some studies of triggered whistler emissions, *J. Geophys. Res.*, *76*(28), 6915–6931, doi:10.1029/JA076i028p06915.

Furuya, N., Y. Omura, and D. Summers (2008), Relativistic turning acceleration of radiation belt electrons by whistler mode chorus, *J. Geophys. Res.*, *113*, A04224, doi:10.1029/2007JA012478.

Gendrin, R. (1981), General relationships between wave amplification and particle diffusion in a magnetoplasma, *Rev. Geophys.*, *19*(1), 171–184, doi:10.1029/RG019i001p00171.

Gibby, A. (2008), Saturation effects in VLF triggered emissions, Stanford University, Stanford, Calif.

Gibby, A. R., U. S. Inan, and T. F. Bell (2008), Saturation effects in the VLF-triggered emission process, *J. Geophys. Res.*, *113*, A11215, doi:10.1029/2008JA013233.

Glauert, S. A., and R. B. Horne (2005), Calculation of pitch angle and energy diffusion coefficients with the PADIE code, *J. Geophys. Res.*, *110*, A04206, doi:10.1029/2004JA010851.

Gołkowski, M., U. S. Inan, A. R. Gibby, and M. B. Cohen (2008), Magnetospheric amplification and emission triggering by ELF/VLF waves injected by the 3.6 MW HAARP ionospheric heater, *J. Geophys. Res.*, *113*, A10201, doi:10.1029/2008JA013157.

Gołkowski, M., U. S. Inan, M. B. Cohen, and A. R. Gibby (2010), Amplitude and phase of nonlinear magnetospheric wave growth excited by the HAARP HF heater, *J. Geophys. Res.*, *115*, A00F04, doi:10.1029/2009JA014610.

Gołkowski, M., M. B. Cohen, D. Carpenter, and U. Inan (2011), On the occurrence of ground observations of ELF/VLF magnetospheric amplification induced by the HAARP facility, *J. Geophys. Res.*, *116*, A04208, doi:10.1029/2010JA016261.

Haque, N., U. S. Inan, T. F. Bell, J. S. Pickett, J. G. Trotignon, and G. Facskó (2011), Cluster observations of whistler mode ducts and banded chorus, *Geophys. Res. Lett.*, *38*, L18107, doi:10.1029/2011GL049112.

Helliwell, R. A. (1965), *Whistlers and Related Ionospheric Phenomena*, Stanford Univ. Press, Stanford, Calif.

Helliwell, R. A. (1988), VLF wave stimulation experiments in the magnetosphere from Siple station, Antarctica, *Rev. Geophys.*, *26*(3), 551–578, doi:10.1029/RG026i003p00551.

Hikishima, M., Y. Omura, and D. Summers (2010), Self-consistent particle simulation of whistler mode triggered emissions, *J. Geophys. Res.*, *115*, A12246, doi:10.1029/2010JA015860.

Inan, U. S. (1987), Gyroresonant pitch angle scattering by coherent and incoherent whistler mode waves in the magnetosphere, *J. Geophys. Res.*, *92*(A1), 127–142, doi:10.1029/JA092iA01p00127.

Inan, U. S., T. F. Bell, and R. A. Helliwell (1978), Nonlinear pitch angle scattering of energetic electrons by coherent VLF waves in the magnetosphere, *J. Geophys. Res.*, *83*(A7), 3235–3253, doi:10.1029/JA083iA07p03235.

Inan, U. S., T. F. Bell, and H. C. Chang (1982), Particle precipitation induced by short-duration VLF waves in the magnetosphere, *J. Geophys. Res.*, *87*, 6243–6264, doi:10.1029/JA087iA08p06243.

Inan, U. S., T. F. Bell, J. Bortnik, and J. M. Albert (2003), Controlled precipitation of radiation belt electrons, *J. Geophys. Res.*, *108*(A5), 1186, doi:10.1029/2002JA009580.

Katoh, Y., and Y. Omura (2007), Computer simulation of chorus wave generation in the Earth's inner magnetosphere, *Geophys. Res. Lett.*, *34*, L03102, doi:10.1029/2006GL028594.

Kennel, C. F., and F. Engelmann (1966), Velocity space diffusion from weak plasma turbulence in a magnetic field, *Phys. Fluids*, *9*(12), 2377–2388, doi:10.1063/1.1761629.

Kennel, C. F., and H. E. Petschek (1966), Limit on stably trapped particle fluxes, *J. Geophys. Res.*, *71*, 1–28.

Li, W., J. Bortnik, R. Thorne, and V. Angelopoulos (2011), Global distribution of wave amplitudes and wave normal angles of chorus waves using THEMIS wave observations, *J. Geophys. Res.*, *116*, A12205, doi:10.1029/2011JA017035.

Lorentzen, K. R., J. B. Blake, U. S. Inan, and J. Bortnik (2001), Observations of relativistic electron microbursts in association with VLF chorus, *J. Geophys. Res.*, *106*, 6017–6028, doi:10.1029/2000JA003018.

Lyons, L. R. (1974), Pitch angle and energy diffusion coefficients from resonant interactions with ion-cyclotron and whistler waves, *J. Plasma Phys.*, *12*, 417–432, doi:10.1017/S002237780002537X.

Lyons, L. R., R. M. Thorne, and C. F. Kennel (1972), Pitch-angle diffusion of radiation belt electrons within the plasmasphere, *J. Geophys. Res.*, *77*(19), 3455–3474, doi:10.1029/JA077i019p03455.

Matsumoto, H., and Y. Omura (1981), Cluster and channel effect phase bunchings by whistler waves in the nonuniform geomagnetic field, *J. Geophys. Res.*, *86*(A2), 779–791, doi:10.1029/JA086iA02p00779.

Nunn, D. (1974), A self-consistent theory of triggered VLF emissions, *Planet. Space Sci.*, *22*, 349–378, doi:10.1016/0032-0633(74)90070-1.

Nunn, D., and Y. Omura (2011), The theory and numerical modelling of non linear wave particle interactions in oblique whistlers, in *General Assembly and Scientific Symposium*, *2011 XXXth URSI*, p. 1, IEEE, Istanbul, doi:10.1109/URSIGASS.2011.6051073.

Omura, Y., and D. Nunn (2011), Triggering process of whistler mode chorus emissions in the magnetosphere, *J. Geophys. Res.*, *116*, A05205, doi:10.1029/2010JA016280.

Omura, Y., H. Matsumoto, D. Nunn, and M. J. Rycroft (1991), A review of observational, theoretical and numerical studies of VLF triggered emissions, *J. Atmos. Terr. Phys.*, *53*, 351–368.

Omura, Y., Y. Katoh, and D. Summers (2008), Theory and simulation of the generation of whistler-mode chorus, *J. Geophys. Res.*, *113*, A04223, doi:10.1029/2007JA012622.

Park, C. G. (1981), Generation of whistler-mode sidebands in the magnetosphere, *J. Geophys. Res.*, *86*(A4), 2286–2294, doi:10.1029/JA086iA04p02286.

Roux, A., and R. Pellat (1978), A theory of triggered emissions, *J. Geophys. Res.*, *83*(A4), 1433–1441, doi:10.1029/JA083iA04p01433.

Shprits, Y. Y., R. M. Thorne, R. B. Horne, and D. Summers (2006), Bounce-averaged diffusion coefficients for field-aligned chorus waves, *J. Geophys. Res.*, *111*, A10225, doi:10.1029/2006JA011725.

Speiser, T. W. (1965), Particle trajectories in a model current sheet, based on the open model of the magnetosphere, with applications to auroral particles, *J. Geophys. Res.*, *70*(7), 1717–1728, doi:10.1029/JZ070i007p01717.

Steinacker, J., and J. A. Miller (1992), Stochastic gyroresonant electron acceleration in a low-beta plasma. I—Interaction with parallel transverse cold plasma waves, *Astrophys. J.*, *393*, 764–781.

Summers, D. (2005), Quasi-linear diffusion coefficients for field-aligned electromagnetic waves with applications to the magnetosphere, *J. Geophys. Res.*, *110*, A08213, doi:10.1029/2005JA011159.

Tao, X., J. Bortnik, J. M. Albert, and R. M. Thorne (2012), Comparison of bounce-averaged quasi-linear diffusion coefficients for parallel propagating whistler mode waves with test particle simulations, *J. Geophys. Res.*, *117*, A10205, doi:10.1029/2012JA017931.

Tao, X., J. Bortnik, J. Albert, R. Thorne, and W. Li (2013), The importance of amplitude modulation in nonlinear interactions between electrons and large amplitude whistler waves, *J. Atmos. Sol. Terr. Phys.*, *99*, 67–72, doi:10.1016/j.jastp.2012.05.012, dynamics of the Complex Geospace System.